Ordinary state-based peridynamic homogenization of periodic micro-structured materials

Wenxuan Xia, Erkan Oterkus* and Selda Oterkus

PeriDynamics Research Centre, Department of Naval Architecture, Ocean and Marine Engineering, University of Strathclyde, Glasgow, United Kingdom

*corresponding author: erkan.oterkus@strath.ac.uk

Abstract

In this work, an ordinary state-based peridynamic homogenization method is presented, in which periodic boundary condition is enforced by coupling the displacement of periodic point pairs. Effective material properties are obtained from the peridynamic displacement gradient tensor. The governing equation of peridynamics is in integro-differential form instead of more common spatial differential form, which grants it unique advantage in performing homogenization analysis involving defects. Recently, with the rapid advancement in additive manufacturing technology, micro-structured materials have attracted significant attention. Microscopic defects occurring during manufacturing process can have a noticeable impact on the overall material behavior especially on the fracture strength of the material. The current study provides a new approach to obtain the effective properties of periodic micro-structured materials with defects.

Keywords: Peridynamics; Homogenization; Periodic boundary condition; Ordinary state-based

1. Introduction

Micro-structured materials have attracted significant attention during the last few years with the advancement in additive manufacturing technology. Microstructural properties of micro-structured materials can be very influential on the overall material behavior especially on the fracture strength of the material. Many periodic micro-structured materials are prone to defects such as voids and cracks during the manufacturing process, which can lead to nonlinear phenomena such as void growth, crack propagation and interfacial debonding. Such microscopic events can have a significant impact on the general elastic response of the periodic material under certain loading conditions, leading to a weakened structure which might be vulnerable to macroscopic failure. The heterogeneous nature of the periodic micro-structured material makes it difficult to perform direct numerical analysis with a complete description of each and every microscopic structural details. The presence of defect further complicates the situation. Therefore, it is important to come up with a homogeneous macroscopic material description to simplify the problem.

Many homogenization methods have been developed over the past few decades to address this issue. Simple operations like direct volume average are simple to implement with little computational cost. Methods of Voigt (stiffness) and Reuss (compliance) mixing rules can reveal useful micromechanical properties such as the upper and lower bounds of the effective material properties. Those types of methods are often referred to as the rules of mixtures (ROM), which are widely used in industry and received further development [1][2]. However, such direct average homogenization treatments become inadequate when structure develops non-linearity. More sophisticated micromechanical approaches utilizing methods such as conventional finite element method (FEM), boundary element method and extended finite element method (XFEM) are developed. For example, the mainstream representative volume element method (RVE), which becomes very popular in industry recently and even has its own extended software support in commercial software such as ANSYS and ABAQUS. On the other hand, mathematical approaches such as asymptotic homogenization theory which uses a two-scale formulation [3] is also becoming increasingly popular despite its less friendly mathematical expression. However, all those methods have their own problems when dealing with microscopic defects although some might prove to be more capable of coping with non-linearity than others. In general, displacement becomes discontinuous once defect appears in the structure and this usually requires new crack tip elements to be accommodated into the

mesh [4] in conjunction with appropriate crack propagation criteria and stress monitoring during the crack propagation process.

Unlike most traditional methods, peridynamics [5] is a meshless approach and can be effectively used in numerical homogenization with defects since peridynamic equations are based on integro-differential equations and do not contain any spatial derivatives. Peridynamic equations are always valid regardless of discontinuities. Defect evolution can be achieved by simply breaking bonds between material points. There has been a rapid progress on peridynamics during the recent years. Peridynamics is utilized for the analysis of composite materials [6-11], polycrystalline materials [12-15] and graphene [16], impact analysis [17,18], fatigue analysis [19,20], analysis of microcrack-macrocrack interactions [21,22], beam and plate analysis [23-26], topology optimization of cracked structures [27], analysis of dynamic fracture [28,29] and analysis of other physical fields [32-35]. An extensive review of peridynamics research is provided by Javili et. al. [36]. A new variation of bond-based peridynamics homogenization method which removed some major limitations from the original bond-based peridynamics theory is previously developed by Madenci et al. [30]. Bond-based peridynamics homogenization is also investigated in [31] recently.

In the current study, a new ordinary state-based peridynamics homogenization method is presented. Unlike traditional bond-based peridynamics which has some limitations on material constants, ordinary state-based peridynamics does not have those limitations. Because of the integro-differential form of its governing equation, ordinary state-based peridynamics is extremely capable at solving homogenization problems with discontinuities.

The numerical results include first the verification of this approach by comparing homogenized properties of common composite materials with several other homogenization approaches. Then the macroscopic material property of some typical crack scenarios is investigated and compared against analytical solutions. Finally, some more complex scenarios with multiple randomly distributed cracks are studied using the current method. It demonstrates a new, flexible, and reliable alternative in solving macroscopic material properties with defects.

2. Ordinary state-based peridynamic formulation

The equation of motion in peridynamics introduced in Silling [5] and later generalized in Silling et al. [37] is a nonlinear integro-differential equation. As shown in [9], the equation of motion can be written as

$$\rho(\mathbf{x})\ddot{\mathbf{u}}(\mathbf{x},t)=\int_{H_{\mathbf{x}}}\left[\mathbf{t}(\mathbf{u}'-\mathbf{u},\mathbf{x}'-\mathbf{x},t)-\mathbf{t}'(\mathbf{u}-\mathbf{u}',\mathbf{x}-\mathbf{x}',t)\right]dV'+\mathbf{b}(\mathbf{x},t) \tag{1a}$$

in which $\mathbf{u}$ and $\mathbf{u}'$ represent displacements of material points located at $\mathbf{x}$ and $\mathbf{x}'$, respectively. H_k defines the horizon (family) of the material point located at $\mathbf{x}$ and its size is specified by the parameter δ. The locality of interactions depends on horizon size and the interactions become more local as δ decreases. Hence, the classical theory of elasticity can be considered as a limiting case of the peridynamic theory as the horizon size approaches zero [38]. ρ, $\ddot{\mathbf{u}}$ and $\mathbf{b}$ are density, acceleration, and body force, respectively. $\mathbf{t}$ and $\mathbf{t}'$ are peridynamic force density vectors between two material points.

Eq. (1a) can be written in the discretized form as [9]

$$\rho(\mathbf{x}_k)\ddot{\mathbf{u}}(\mathbf{x}_k,t)=\sum_{j=1}^{N}\left[\mathbf{t}_{kj}\left(\mathbf{u}_j-\mathbf{u}_k,\mathbf{x}_j-\mathbf{x}_k,t\right)-\mathbf{t}_{jk}\left(\mathbf{u}_k-\mathbf{u}_j,\mathbf{x}_k-\mathbf{x}_j,t\right)\right]V_j+\mathbf{b}(\mathbf{x}_k,t) \tag{1b}$$

in which N is the total number of material points located within the horizon of the material point k and V_j represents the incremental volume of material point j.

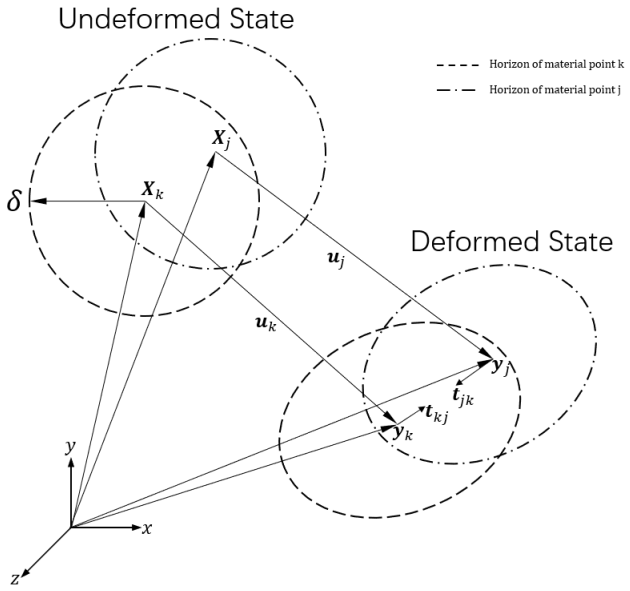

Fig. 1. Deformed ordinary state-based peridynamics configuration in comparison to its undeformed state and resulted pairwise force densities.

As shown in Fig. 1, material point k interacts with its family members within its horizon and is influenced by the collective deformation of all its family members, hence producing the force density vector $\mathbf{t}_{kj}$, acting at material point k. Likewise, material j is also influenced by the deformation of all material points within its horizon. The positions of material points k and j in the deformed state are specified by $\mathbf{y}_k = \mathbf{x}_k + \mathbf{u}_k$ and $\mathbf{y}_j = \mathbf{x}_j + \mathbf{u}_j$, respectively.

The pairwise force density vectors $\mathbf{t}_{kj}$ and $\mathbf{t}_{jk}$ satisfy the requirement for balance of angular momentum, therefore can be expressed as follows [9]

$$\mathbf{t}_{kj}\left(\mathbf{u}_j - \mathbf{u}_k, \mathbf{x}_j - \mathbf{x}_k, t\right) = \frac{1}{2} A \frac{\mathbf{y}_j - \mathbf{y}_k}{\left|\mathbf{y}_j - \mathbf{y}_k\right|} \tag{2a}$$

$$\mathbf{t}_{jk}\left(\mathbf{u}_k - \mathbf{u}_j, \mathbf{x}_k - \mathbf{x}_j, t\right) = -\frac{1}{2} B \frac{\mathbf{y}_j - \mathbf{y}_k}{\left|\mathbf{y}_j - \mathbf{y}_k\right|} \tag{2b}$$

in which A and B are auxiliary parameters that are dependent on material constants, displacement field and horizon size. The relationship between the force density vector and the strain energy density can be expressed as [9]

$$\mathbf{t}_{kj}\left(\mathbf{u}_j - \mathbf{u}_k, \mathbf{x}_j - \mathbf{x}_k, t\right) = \frac{1}{V_j} \frac{\partial W_k}{\partial\left(\left|\mathbf{y}_j - \mathbf{y}_k\right|\right)} \frac{\mathbf{y}_j - \mathbf{y}_k}{\left|\mathbf{y}_j - \mathbf{y}_k\right|} \tag{3}$$

Interaction between two material points results in pairwise force vectors $\mathbf{t}_{kj}$ and $\mathbf{t}_{jk}$. Change in distance between interacting material points k and j causes micro-potential residing within the bond. Integrating micro-potentials over all bonds within a horizon produces the strain energy density $W(\mathbf{x}_k)$ in terms of dilatation and distortional components. For a linear isotropic elastic material, the explicit form of the strain energy density can be written as [9]

$$W(\mathbf{x}_k) = a\theta_k^2 + b\sum_{j=1}^{N} \frac{\delta}{|\mathbf{x}_j - \mathbf{x}_k|}\left(|\mathbf{y}_j - \mathbf{y}_k| - |\mathbf{x}_j - \mathbf{x}_k|\right)^2 V_j \tag{4}$$

The dilatation term θ can be expressed as [9]

$$\theta_k = d\sum_{j=1}^{N} \frac{\delta}{|\mathbf{x}_j - \mathbf{x}_k|}\left(|\mathbf{y}_j - \mathbf{y}_k| - |\mathbf{x}_j - \mathbf{x}_k|\right)\left(\frac{\mathbf{y}_j - \mathbf{y}_k}{|\mathbf{y}_j - \mathbf{y}_k|} \cdot \frac{\mathbf{x}_j - \mathbf{x}_k}{|\mathbf{x}_j - \mathbf{x}_k|}\right) V_j \tag{5}$$

The peridynamic parameters, a, b, and d depend on material constants and horizon size. Their expressions for two-dimensional domain are given in [9] as follows

$$a = \frac{1}{2}(\kappa - 2\mu), \quad b = \frac{6\mu}{\pi h \delta^4}, \quad d = \frac{2}{\pi h \delta^3} \tag{6}$$

where κ and μ are the bulk and shear modulus of the material, respectively. The parameter h is the thickness.

For peridynamic bonds extending through at least two different material types, its bond properties depend on the type of materials existing along the path. Material points k and j can be embedded in different materials, in which case the effective micro-modulus of a bond can be evaluated by dividing bond into multiple segments as shown in Fig. 2a

$$a_{kj} = \frac{\sum_{m=1}^{M} d_m}{\sum_{m=1}^{M} \frac{d_m}{a^{(k,j;m)}}} \tag{7a}$$

$$b_{kj} = \frac{\sum_{m=1}^{M} d_m}{\sum_{m=1}^{M} \frac{d_m}{b^{(k,j;m)}}} \tag{7b}$$

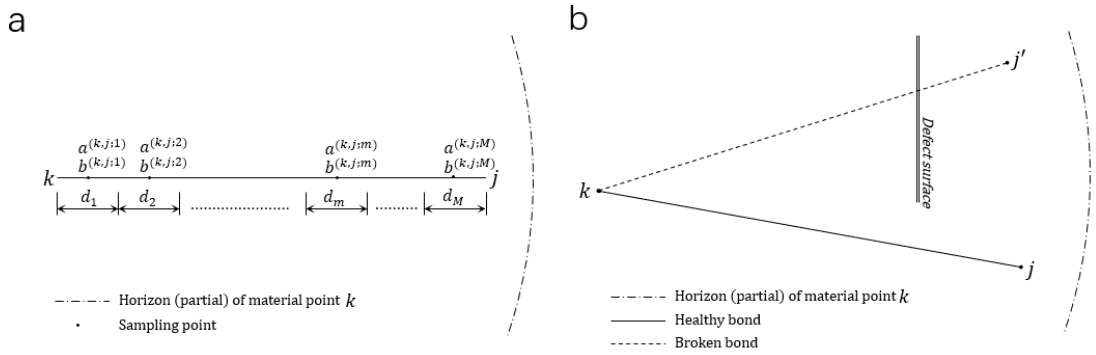

Fig. 2. (a) Peridynamic parameters at dissimilar material interface. **(b)** Bond breakage at defect surface.

d_m represents the length of each segment within a bond kj. The parameter M denotes the total number of segments along the bond path. Peridynamic parameters a and b from Eq. 6 are evaluated for each segment m and are denoted as $a^{(k,j;m)}$ and $b^{(k,j;m)}$. The equivalent micro-modulus a_{kj} and b_{kj} of bond kj are then assembled as shown in Eq.7

The auxiliary parameters A and B in Eq. 2 can be obtained as

$$A = \psi_{kj}^0 4 \frac{\delta}{\left|\mathbf{x}_j - \mathbf{x}_k\right|} \left\{ d \left(\frac{\mathbf{y}_j - \mathbf{y}_k}{\left|\mathbf{y}_j - \mathbf{y}_k\right|} \cdot \frac{\mathbf{x}_j - \mathbf{x}_k}{\left|\mathbf{x}_j - \mathbf{x}_k\right|} \right) a\theta_k + b\left(\left|\mathbf{y}_j - \mathbf{y}_k\right| - \left|\mathbf{x}_j - \mathbf{x}_k\right| \right) \right\} \tag{8a}$$

$$B = \psi_{kj}^0 4 \frac{\delta}{\left|\mathbf{x}_k - \mathbf{x}_j\right|} \left\{ d \left(\frac{\mathbf{y}_j - \mathbf{y}_k}{\left|\mathbf{y}_j - \mathbf{y}_k\right|} \cdot \frac{\mathbf{x}_j - \mathbf{x}_k}{\left|\mathbf{x}_j - \mathbf{x}_k\right|} \right) a\theta_j + b\left(\left|\mathbf{y}_k - \mathbf{y}_j\right| - \left|\mathbf{x}_k - \mathbf{x}_j\right| \right) \right\} \tag{8b}$$

in which the parameter ψ_{kj}^0 controls the initial failure of the bond between material points k and j due to pre-existing cracks as shown in Fig. 2b

$$\psi_{kj}^0 = \begin{cases} 0 & \text{if bond intersects with a preexisting crack} \\ 1 & \text{otherwise} \end{cases} \tag{9}$$

3. Representative volume element formulation

If the microscopic detail of a heterogeneous material can be defined by a representative volume element (RVE) for a statistically homogeneous medium, microscopic analysis can be

performed to obtain a homogenized description for this material. At least two distinct scales coexist in the process of homogenization: the macroscopic scale (x) and the microscopic scale (y). For illustrative purposes, we will only consider linear elastic deformation in this study. The constitutive relations for the original heterogeneous material can be assumed as [10]

$$\boldsymbol{\sigma} = \mathbf{C} \cdot \boldsymbol{\varepsilon} \tag{10a}$$

$$\boldsymbol{\varepsilon} = \mathbf{S} \cdot \boldsymbol{\sigma} \tag{10b}$$

where $\mathbf{C}$ and $\mathbf{S}$ are functions of location that called stiffness tensor and compliance tensor, respectively. Stiffness tensor is the inverse of compliance tensor, $\mathbf{C} = \mathbf{S}^{-1}$. $\boldsymbol{\sigma}$ and $\boldsymbol{\varepsilon}$ are called microscopic stress field and microscopic strain field, respectively.

If we assume the microstructure of a composite as periodic, the micromechanical analysis can be performed within a unit cell (UC). Any individual UC can be effectively approximated as a material point in the macroscopic analysis. Homogenization replaces the original heterogeneous material with a fictitious homogeneous medium which has the constitutive relations of [10]

$$\bar{\boldsymbol{\sigma}} = \mathbf{C}^* \cdot \bar{\boldsymbol{\varepsilon}} \tag{11a}$$

$$\bar{\boldsymbol{\varepsilon}} = \mathbf{S}^* \cdot \bar{\boldsymbol{\sigma}} \tag{11b}$$

in which $\mathbf{C}^*$ and $\mathbf{S}^*$ are called effective stiffness tensor and effective compliance tensor, respectively, which also satisfy the relationship of $\mathbf{C}^* = \mathbf{S}^{*-1}$. $\bar{\boldsymbol{\sigma}}$ and $\bar{\boldsymbol{\varepsilon}}$ are called macroscopic stress and strain, respectively, which are constant values within a cell's domain.

It is assumed that the macroscopic displacement field $\bar{\mathbf{u}}$ can be expressed in terms of the microscopic displacement field $\mathbf{u}$ as [10]

$$\bar{\mathbf{u}} = \frac{1}{V}\int \mathbf{u}\, dV \tag{12}$$

where V represents the volume of the UC. Microscopic displacement field $\mathbf{u}$ can be expressed in terms of volume averaged displacement field $\bar{\mathbf{u}}$ and displacement fluctuation function $\tilde{\mathbf{u}}$ as

$$\mathbf{u} = \bar{\mathbf{u}} + \bar{\boldsymbol{\varepsilon}} \cdot x + \tilde{\mathbf{u}} \tag{13}$$

in which $\bar{\boldsymbol{\varepsilon}}$ is the average strain vector defined as

$$\bar{\boldsymbol{\varepsilon}} = \frac{\partial \bar{\mathbf{u}}}{\partial x} \tag{14}$$

According to average stress and strain theorem, the volume average of the stress or strain field inside the body is equal to the constant stress or strain tensor along the border, respectively, which can be expressed as [10]

$$\frac{1}{V}\int \boldsymbol{\sigma} dV = \bar{\boldsymbol{\sigma}} \tag{15a}$$

$$\frac{1}{V}\int \boldsymbol{\varepsilon} dV = \bar{\boldsymbol{\varepsilon}} \tag{15b}$$

in which the constant stress or strain tensor $\bar{\sigma}_{ij}$ is applied on a fictitious boundary region in

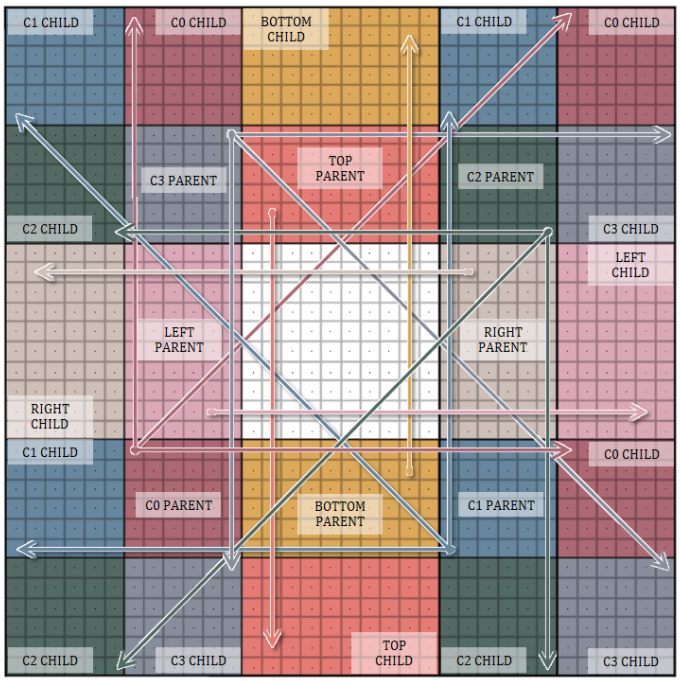

Fig. 3. Peridynamic point coupling for periodic boundary condition.

peridynamic analysis. A periodic boundary region relation is established as shown in Fig. 3. Outer regions labeled as "Child" are fictitious. Child points populate the fictitious region. They do not have their own horizon and family but can be a family point of other non-fictitious points. Neighboring the fictitious regions are eight parent region and material points within those regions are parent points. Each child point is coupled with one parent point. However, for each parent point, there can be multiple subordinate child points. The displacement value of the child point solely depends on the displacement value of its parent point as well as the periodic condition. On the other hand, the displacement of the parent point is resulted from the collective influence of all material points within its horizon, regardless of fictitious or not. The size of the fictitious region should be larger than two times the horizon size δ. Therefore, the

family will be complete for all material points within the integration domain and the periodic condition is satisfied.

The periodic relationship between parent and child points can be expressed as

$$\mathbf{u}_i^c = \mathbf{u}_i^p + \bar{\boldsymbol{\varepsilon}}_{ij}\left(\mathbf{x}_j^c - \mathbf{x}_j^p\right) \tag{16}$$

in which $\mathbf{u}$ is the displacement. Superscripts c and p represent the corresponding child and parent component of each point-pair as shown in Fig. 3. $\bar{\boldsymbol{\varepsilon}}_{ij}$ is the macroscopic strain. When applying Eq. (16) in numerical analysis, the displacement of child point is being calculated based on Eq. (16) since the child point does not have its own horizon. The displacement of the child point depends on its initial location, the initial location of its parent point, the displacement of its parent point and the macroscopic strain $\bar{\boldsymbol{\varepsilon}}_{ij}$. After solving Eq. (16), the relationship between child displacement and parent displacement is obtained. For explicit analysis, parent displacement field is obtained first, then child point displacement can be obtained through Eq. (16), after that the current timestep is considered complete. If implicit analysis is implemented, method of Langrage multiplier can be used to incorporate Eq. (16) of every point pairs into linear system, then an iterative solver is recommended in obtaining the final displacement solution.

From Eq. (13) and periodic boundary condition stated in Eq. (16), the microscopic strain field $\boldsymbol{\varepsilon}$ can be obtained as

$$\boldsymbol{\varepsilon} = \bar{\boldsymbol{\varepsilon}} + \tilde{\boldsymbol{\varepsilon}} \tag{17}$$

If we substitute Eq. (15) into the constitutive relations given in Eq. (11), the relationship between microscopic stress and macroscopic strain can be obtained as

$$\mathbf{C}^* \bar{\boldsymbol{\varepsilon}} = \frac{1}{V}\int \boldsymbol{\sigma} dV \tag{18}$$

in which the macroscopic strain $\bar{\boldsymbol{\varepsilon}}$ is applied to the cell as boundary condition and can be defined as

$$\bar{\boldsymbol{\varepsilon}}_1^T = \left[c_s, 0, 0, 0, 0, 0\right] \tag{19a}$$

$$\bar{\boldsymbol{\varepsilon}}_2^T = \left[0, c_s, 0, 0, 0, 0\right] \tag{19b}$$

$$\bar{\boldsymbol{\varepsilon}}_3^T = \left[0, 0, c_s, 0, 0, 0\right] \tag{19c}$$

$$\bar{\boldsymbol{\varepsilon}}_4^T = \left[0,0,0,c_s/2,0,0\right] \tag{19d}$$

$$\bar{\boldsymbol{\varepsilon}}_5^T = \left[0,0,0,0,c_s/2,0\right] \tag{19e}$$

$$\bar{\boldsymbol{\varepsilon}}_6^T = \left[0,0,0,0,0,c_s/2\right] \tag{19f}$$

In which c_s is a small scalar controlling the magnitude of the macroscopic strain.

The microscopic stress tensor $\boldsymbol{\sigma}$ can be obtained from the displacement-based homogenization result. As derived by Gu et. al. [39], the peridynamic stress tensor $\boldsymbol{\sigma}$ can be expressed in terms of the displacement gradient tensor $\nabla\mathbf{u}$ and material constants E, v for linear isotropic material as

$$\boldsymbol{\sigma} = \frac{Ev}{(1+v)(1-2v)}\left[tr\left(\nabla\mathbf{u}\right)\right]\mathbf{I} + \frac{E}{2(1+v)}\left[\nabla\mathbf{u} + \left(\nabla\mathbf{u}\right)^T\right] \tag{20}$$

in which $\mathbf{I}$ is the identity matrix. The displacement gradient tensor $\nabla\mathbf{u}$ can be expressed as

$$\nabla\mathbf{u}_k = \left\{\int_{H_k} \frac{\delta}{\left|\mathbf{x}_j - \mathbf{x}_k\right|}\left[\left(\mathbf{u}_j - \mathbf{u}_k\right)\otimes\left(\mathbf{x}_j - \mathbf{x}_k\right)\right]dV_j\right\}\mathbf{K}^{-1} \tag{21}$$

where $\otimes$ denotes the dyadic product, $\dfrac{\delta}{\left|\mathbf{x}_j - \mathbf{x}_k\right|}$ is a scalar field acting as an influence function, and $\mathbf{K}$ is the shape tensor defined as [39]

$$\mathbf{K}\left(\mathbf{x}_k\right) = \int_{H_k} \frac{\delta}{\left|\mathbf{x}_j - \mathbf{x}_k\right|}\left[\left(\mathbf{x}_j - \mathbf{x}_k\right)\otimes\left(\mathbf{x}_j - \mathbf{x}_k\right)\right]dV_j \tag{22}$$

Finally, the effective stiffness tensor $\mathbf{C}^*$ can be assembled column by column from the peridynamic stress tensor $\boldsymbol{\sigma}$ and the macroscopic strain $\bar{\boldsymbol{\varepsilon}}$ as

$$\begin{Bmatrix} C_{1,i} \\ C_{2,i} \\ C_{3,i} \\ C_{4,i} \\ C_{5,i} \\ C_{6,i} \end{Bmatrix} = \begin{Bmatrix} \left\langle \sigma_i^{xx} \right\rangle \\ \left\langle \sigma_i^{yy} \right\rangle \\ \left\langle \sigma_i^{zz} \right\rangle \\ \left\langle \sigma_i^{yz} \right\rangle \\ \left\langle \sigma_i^{zx} \right\rangle \\ \left\langle \sigma_i^{xy} \right\rangle \end{Bmatrix} / c_s, \quad \left(i = 1,\ldots,6\right) \tag{23}$$

where the angle bracket denotes the volume average over cell domain.

4. Numerical analysis

The current method is verified by considering the homogenization result of a boron aluminum composite cell as shown in Fig. 4. The peridynamic predictions of the elastic moduli are compared with analytical solutions and available numerical data provided in [40][41][42]. The constituent properties for the boron aluminum composite are given in Table 1. In numerical analysis, a two-dimensional unit cell is considered. 120 by 120 peridynamic material point discretization is used in this analysis, and circular horizon with δ equivalent to 3 times of discretization size is chosen. Effective material properties were calculated by using Eqs. (18)-(23). As shown in Table 2, a good agreement is observed between peridynamic homogenization and other homogenization methods in terms of effective Elastic moduli and Poisson's ratio.

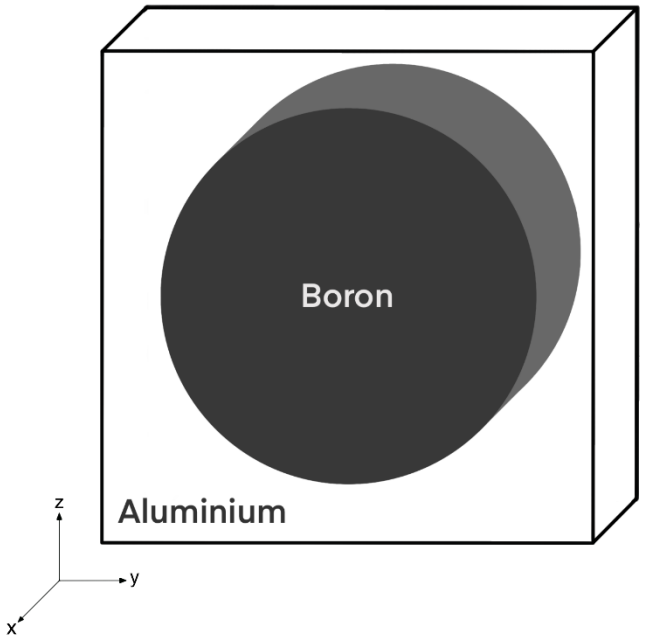

Fig. 4. Boron aluminum composite cell.

Table 1. Constituent properties for boron and aluminum composite

Material name	Elastic modulus E (GPa)	Poisson's Ratio v	Volume fraction
Boron	379.3	0.1	0.47
Aluminum	68.3	0.3	0.53

Table 2. Elastic moduli for boron aluminum composite

	E_2 (GPa)	G_{12} (GPa)	v_{12}
Ordinary state-based peridynamics	150	53.4	0.18
Sun and Vaidya [40]	144	57.2	0.19
Sun and Chen [41]	135	51.1	0.19
Chamis [40]	156	62.6	0.20
Whitney et al. [42]	123	53.9	0.19

The following examples concern the softening of effective elastic response of a two-dimensional matrix cell. The elastic material parameters of the matrix are: Elastic modulus $E = 2\times10^9$ Pa and Poisson's ratio $v = 0.3$. The cell geometry is considered of unit dimension. As shown in Fig. 5, we consider two distinct scenarios of crack arrangement. In the first scenario, a single crack is embedded horizontally at the center of the cell. In the second scenario, two coalescing cracks are arranged horizontally at their corresponding initial locations. In order to isolate the crack homogenization aspect of the problem and achieve a more constructive benchmark for verification, a quasi-static cracking procedure is assumed, in which crack path is restricted to a straight path horizontally. This crack process is identical to the referenced analytical solution. Both cases start with total crack length equals to zero and end up with total crack length equals to cell width. This means that the vertical effective elastic property of the cell will be equal to the matrix property and reaches zero at the end of the cracking process. Twenty steps are evenly distributed throughout the cracking process for both scenarios. Parameter C_{2222} from the effective material property matrix C^* is compared with the analytical solution from [43].

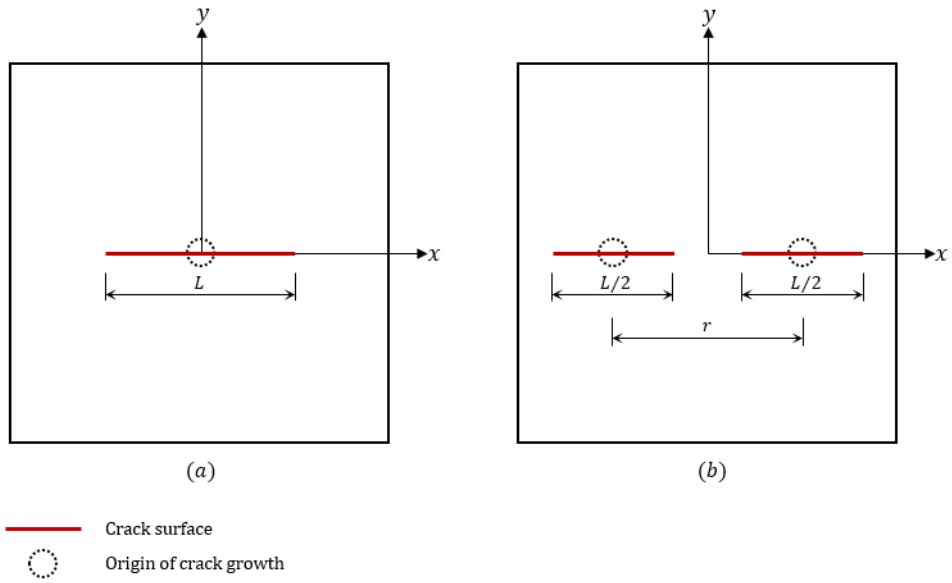

Fig. 5. (a) single crack matrix cell; **(b)** coalescing cracks matrix cell.

Parameter r in Fig. 5 (b) is the distance between the origins of cracks and is set equal to 0.25 hence causing the cracks to merge at $L = 0.5$ creating a sudden decrease in y directional cell effective strength. L is the total length of the cracks. The two crack benchmark problems are solved with a 70x70 peridynamic discretization. Circular horizon with δ equivalent to 3 times of discretization size is chosen. Results are compared against analytical solution in Figs. 6 and 7.

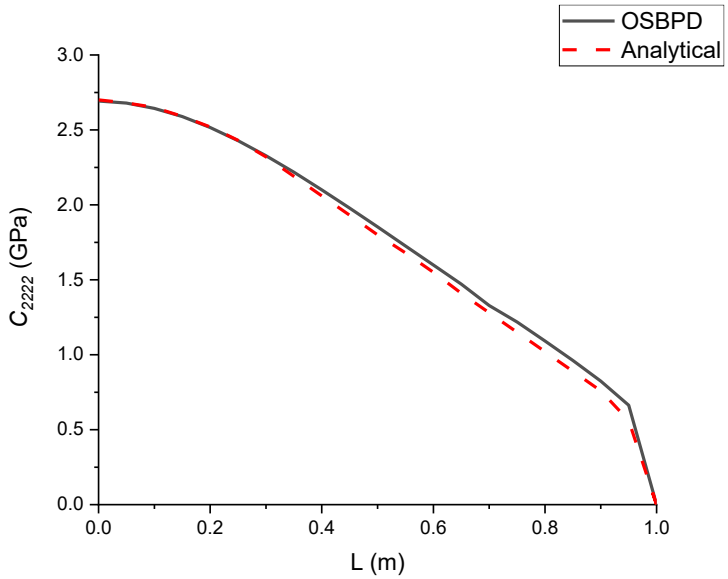

Fig. 6. Predicted effective modulus for single crack cell from ordinary state-based peridynamics (OSBPD) in comparison with analytical results.

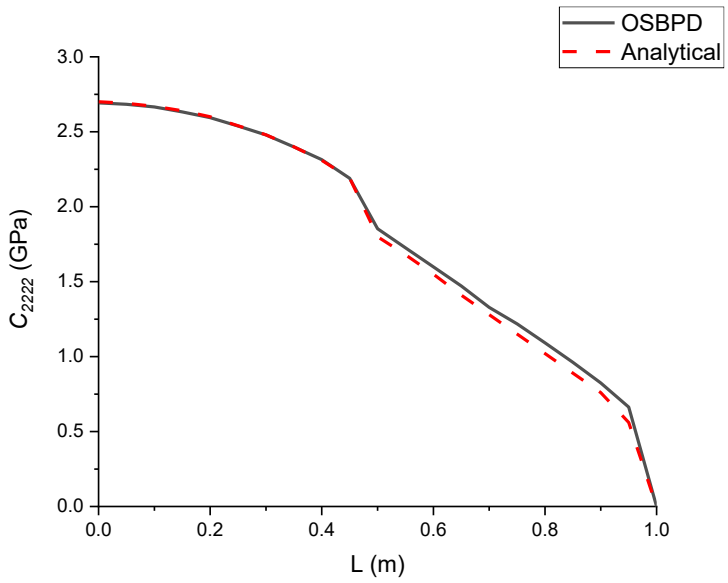

Fig. 7. Predicted effective modulus for coalescing cracks cell from OSBPD in comparison with analytical results.

The peridynamic homogenization results agree well with analytical solutions. For the coalescing cracks scenario, the sudden decrease of the effective modulus when cracks join is accurately captured.

The third and final example investigates a more complex crack setup by considering a matrix cell with multiple random non-intersecting cracks. The effective strength of such a cell is influenced by parameters such as crack orientation, crack density and crack shape etc. The matrix cell geometry is considered to have unit dimension. Let us first define the crack density expression as

$$\rho = Nd^2 / A \tag{28}$$

where N is the total number of cracks, d is the size of an individual crack and A is the surface area of the cell.

Two orientation conditions are considered: horizontally parallel cracks and arbitrarily oriented cracks. For each of these scenarios, six crack densities are considered: ρ = 0.1, 0.2, 0.3, 0.4, 0.5 and 0.6. Crack size d is set to 0.16 in both scenarios. N is rounded into its nearest integer

for simplification. Five instances are generated for each crack density level to obtain average results for comparison.

Cracks are generated with the help of a random number generator. For the first scenario with parallel cracks, the rule governing the crack generation is straightforward: the location of any individual crack is statistically random, any two cracks need to be separated from each other, and cracks should not penetrate outside of cell domain, see Fig. 8.

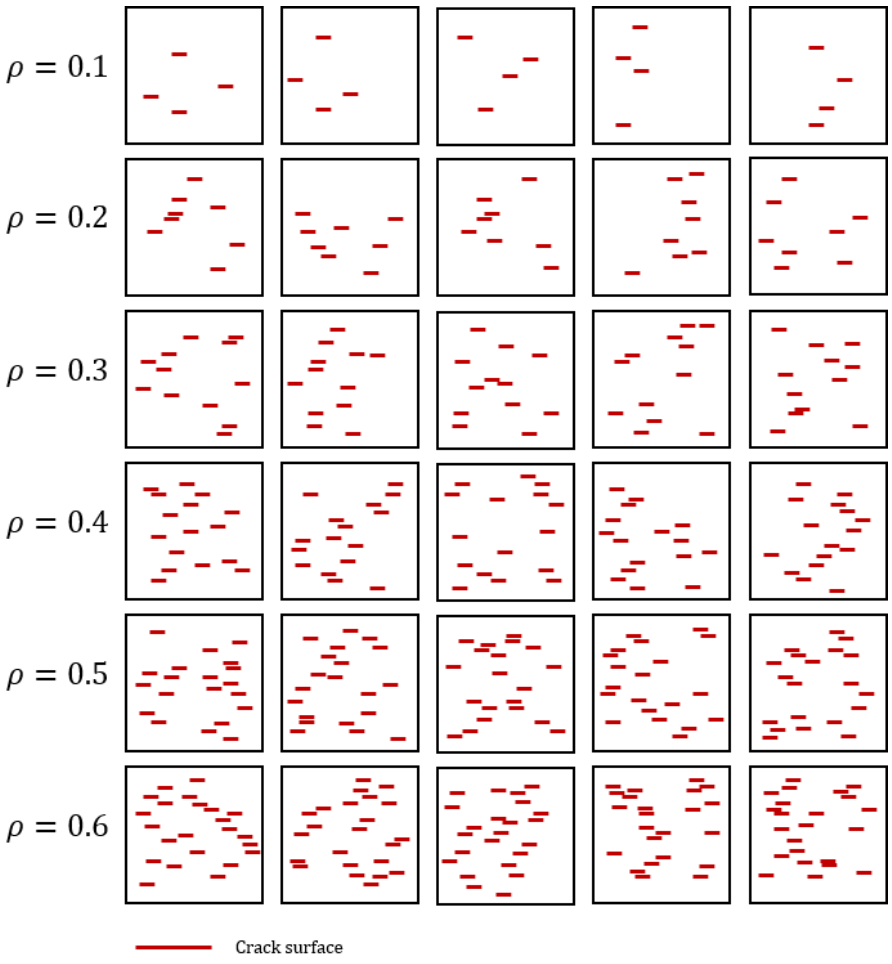

Fig. 8. Random parallel cracks setup

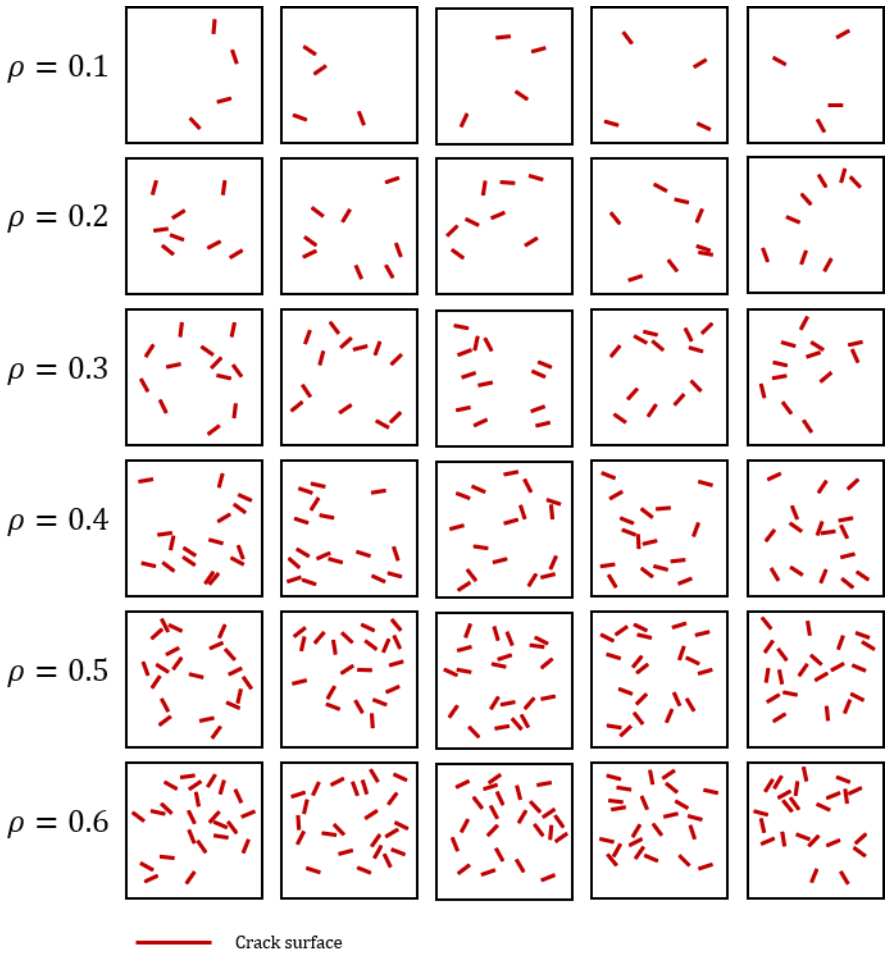

Fig. 9. Random arbitrarily oriented cracks setup

For the second scenario where cracks are orientated arbitrarily, the locations of cracks are statistically random, the orientation is also generated randomly while ensuring later generated cracks do not intersect with existing cracks, and also any crack should not penetrate outside of cell domain, see Fig. 9. For those locations where no acceptable cracks can be generated, a new location will be selected and so forth.

Examples are solved with 60x60 peridynamic discretization. Circular horizon with δ equivalent to 3 times of discretization size is chosen.

Numerical results are shown in Fig. 10 and Fig. 11 where E_v and E_h are reduced effective elastic moduli in vertical direction and horizontal direction, respectively. This elastic modulus softening is a direct result of the crack presence within the cell. The impact is measured by comparing the reduced modulus E_v and E_h against their original undamaged counterpart E_v^0

and E_h^0. The ratio E/E^0 is denoted as a material softening parameter ψ_E. When material softening happens due to the presence of cracks, parameter ψ_E will reduce accordingly.

For the random generated horizontal microcrack case, the effective elastic property in horizontal direction is not influenced by the presence of cracks. However, the effective elastic property in vertical direction decreases while the crack density increase. For the random generated arbitrary oriented microcrack case, the effective elastic property in both horizontal and vertical direction decrease at the same rate while the crack density increase. Horizontal parallel cracks have a larger impact on material's vertical effective elastic strength in comparison to arbitrary orientated cracks.

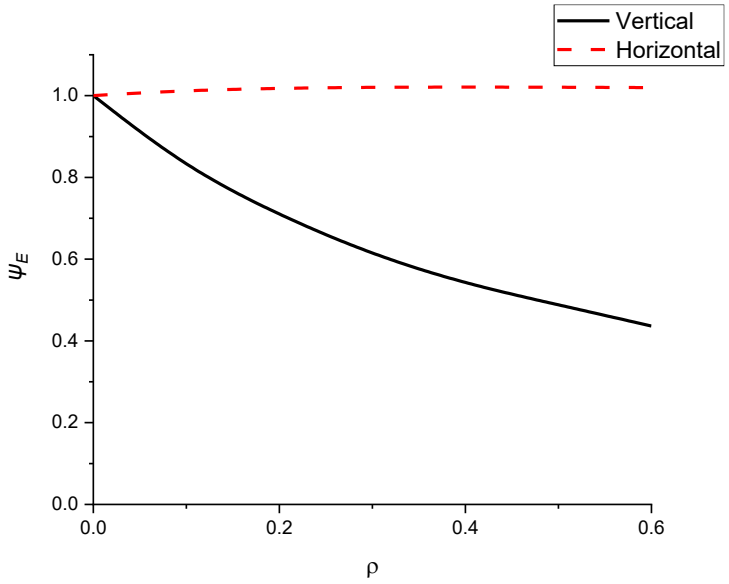

Fig. 10. Elastic modulus softening for randomly distributed parallel cracks with increasing crack density.

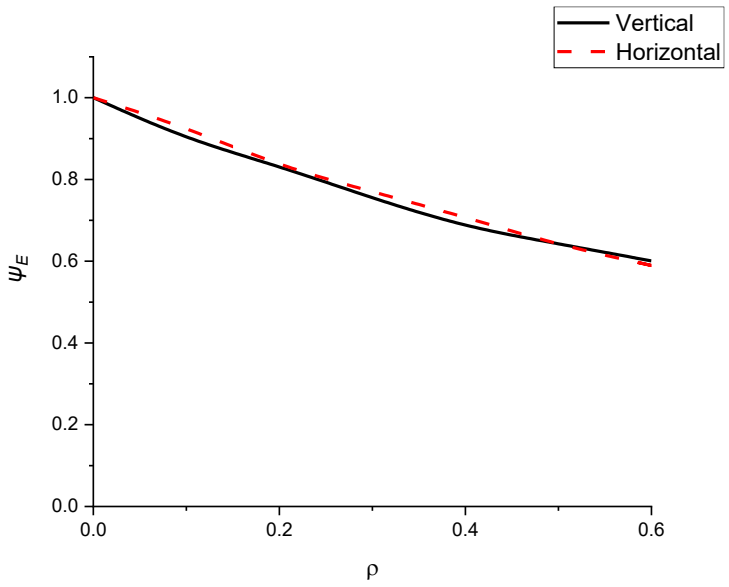

Fig. 11. Elastic modulus softening for randomly distributed arbitrarily orientated cracks with increasing crack density.

5. Conclusion

In this study, a new ordinary state-based peridynamic homogenization method for micro-structured materials with defects is presented. Several benchmark problems are considered including unit sized composite cell and unit cell with cracks. Results of all benchmark problems are verified against analytical solution or referenced numerical study and good agreement is obtained for all cases. Numerical results also investigate the homogenization of multiple random positioned micro-cracks with great success. The current method offers a new alternative for periodic micro-structured material homogenization. The proposed peridynamic periodic boundary relation is also applicable for 3D geometry. Furthermore, the proposed approach can be used effectively for solving fracture problems.

References

[1] Swan, C.C. and Kosaka, I., 1997. Voigt–Reuss topology optimization for structures with linear elastic material behaviours. International Journal for Numerical Methods in Engineering, 40(16), pp.3033-3057.

[2] Kim, H.S., Hong, S.I. and Kim, S.J., 2001. On the rule of mixtures for predicting the mechanical properties of composites with homogeneously distributed soft and hard particles. Journal of Materials Processing Technology, 112(1), pp.109-113.

[3] Fish, J., Shek, K., Pandheeradi, M. and Shephard, M.S., 1997. Computational plasticity for composite structures based on mathematical homogenization: Theory and practice. Computer methods in applied mechanics and engineering, 148(1-2), pp.53-73.

[4] Zi, G. and Belytschko, T., 2003. New crack-tip elements for XFEM and applications to cohesive cracks. International Journal for Numerical Methods in Engineering, 57(15), pp.2221-2240.

[5] Silling, S.A., 2000. Reformulation of elasticity theory for discontinuities and long-range forces. Journal of the Mechanics and Physics of Solids 48(1), 175–209.

[6] Oterkus, E., Barut, A., Madenci, E., 2010. Damage growth prediction from loaded composite fastener holes by using peridynamic theory. In 51st AIAA/ASME/ASCE/AHS/ASC Structures, Structural Dynamics, and Materials Conference 18th AIAA/ASME/AHS Adaptive Structures Conference, Orlando, Florida, USA, p. 3026.

[7] Oterkus, E., Madenci, E., 2012. Peridynamics for failure prediction in composites. In 53rd AIAA/ASME/ASCE/AHS/ASC Structures, Structural Dynamics and Materials Conference 20th AIAA/ASME/AHS Adaptive Structures Conference, Honolulu, Hawaii, USA, p. 1692.

[8] Oterkus, E., Madenci, E., 2012. Peridynamic theory for damage initiation and growth in composite laminate. Key Engineering Materials 488, 355–358.

[9] Madenci, E., Oterkus, E., 2014. Peridynamic theory and its applications. Springer, New York, NY.

[10] Cioranescu, D. and Donato, P., 1999. An introduction to homogenization (Vol. 17). Oxford: Oxford University Press.

[11] Hu, Y.L., Yu, Y. and Madenci, E., 2020. Peridynamic modeling of composite laminates with material coupling and transverse shear deformation. Composite Structures 253, p.112760.

[12] De Meo, D., Zhu, N., Oterkus, E., 2016. Peridynamic modeling of granular fracture in polycrystalline materials. Journal of Engineering Materials and Technology 138(4), 041008.

[13] De Meo, D., Russo, L., Oterkus, E., 2017. Modeling of the onset, propagation, and interaction of multiple cracks generated from corrosion pits by using peridynamics. Journal of Engineering Materials and Technology 139(4), 041001.

[14] Zhu, N., De Meo, D., Oterkus, E., 2016. Modelling of granular fracture in polycrystalline materials using ordinary state-based peridynamics. Materials 9(12), p.977.

[15] Liu, B., Yang, Z. and Bao, R., 2020. The grain orientation effects on crack-tip fields for additively manufactured titanium alloy: A peridynamic study. *Theoretical and Applied Fracture Mechanics*, p.102555.

[16] Liu, X., He, X., Wang, J., Sun, L., Oterkus, E., 2018. An ordinary state-based peridynamic model for the fracture of zigzag graphene sheets. Proceedings of the Royal Society A: Mathematical, Physical and Engineering Sciences 474(2217), p.20180019.

[17] Oterkus, E., Guven, I., Madenci, E., 2012. Impact damage assessment by using peridynamic theory. Open Engineering 2(4), 523–531.

[18] Wu, L., Wang, L., Huang, D. and Xu, Y., 2020. An ordinary state-based peridynamic modeling for dynamic fracture of laminated glass under low-velocity impact. Composite Structures 234, p.111722.

[19] Liu, B., Wang, K., Bao, R. and Sui, F., 2020. The effects of α/β phase interfaces on fatigue crack deflections in additively manufactured titanium alloy: A peridynamic study. International Journal of Fatigue 137, p.105622.

[20] Oterkus, E., Guven, I. and Madenci, E., 2010. Fatigue failure model with peridynamic theory. In 12th IEEE Intersociety Conference on Thermal and Thermomechanical Phenomena in Electronic Systems, Las Vegas, Nevada, USA, p. 1-6.

[21] Vazic, B., Wang, H., Diyaroglu, C., Oterkus, S., Oterkus, E., 2017. Dynamic propagation of a macrocrack interacting with parallel small cracks. AIMS Materials Science 4(1), pp.118–136.

[22] Basoglu, M.F., Zerin, Z., Kefal, A., Oterkus, E., 2019. A computational model of peridynamic theory for deflecting behavior of crack propagation with micro-cracks. Computational Materials Science 162, 33–46.

[23] Diyaroglu, C., Oterkus, E., Oterkus, S., 2019. An Euler–Bernoulli beam formulation in an ordinary state-based peridynamic framework. Mathematics and Mechanics of Solids 24(2), 361–376.

[24] Vazic, B., Oterkus, E., Oterkus, S., 2020. Peridynamic model for a Mindlin plate resting on a Winkler elastic foundation. Journal of Peridynamics and Nonlocal Modeling, pp.1–10.

[25] Yang, Z., Oterkus, E., Nguyen, C.T., Oterkus, S., 2019. Implementation of peridynamic beam and plate formulations in finite element framework. Continuum Mechanics and Thermodynamics 31(1), 301–315.
[26] Yang, Z., Vazic, B., Diyaroglu, C., Oterkus, E., Oterkus, S., 2020. A Kirchhoff plate formulation in a state-based peridynamic framework. Mathematics and Mechanics of Solids 25(3), 727–738.
[27] Kefal, A., Sohouli, A., Oterkus, E., Yildiz, M., Suleman, A., 2019. Topology optimization of cracked structures using peridynamics. Continuum Mechanics and Thermodynamics 31(6), 1645–1672.
[28] Imachi, M., Tanaka, S., Bui, T.Q., Oterkus, S., Oterkus, E., 2019. A computational approach based on ordinary state-based peridynamics with new transition bond for dynamic fracture analysis. Engineering Fracture Mechanics 206, 359–374.
[29] Imachi, M., Tanaka, S., Ozdemir, M., Bui, T.Q., Oterkus, S., Oterkus, E., 2020. Dynamic crack arrest analysis by ordinary state-based peridynamics. International Journal of Fracture 221(2), pp.155–169.
[30] Madenci, E., Barut, A., Phan, N., 2018. Peridynamic unit cell homogenization for thermoelastic properties of heterogenous microstructures with defects. Composite Structures 188, 104–115.
[31] Buryachenko, V.A., 2020. Generalized Mori–Tanaka approach in micromechanics of peristatic random structure composites. Journal of Peridynamics and Nonlocal Modeling, 1–24.
[32] De Meo, D., Oterkus, E., 2017. Finite element implementation of a peridynamic pitting corrosion damage model. Ocean Engineering 135, 76–83.
[33] Diyaroglu, C., Oterkus, S., Oterkus, E., Madenci, E., 2017a. Peridynamic modeling of diffusion by using finite-element analysis. IEEE Transactions on Components, Packaging and Manufacturing Technology 7(11), 1823–1831.
[34] Diyaroglu, C., Oterkus, S., Oterkus, E., Madenci, E., Han, S., Hwang, Y., 2017b. Peridynamic wetness approach for moisture concentration analysis in electronic packages. Microelectronics Reliability 70, 103–111.
[35] Wang, H., Oterkus, E., Oterkus, S., 2018. Predicting fracture evolution during lithiation process using peridynamics. Engineering Fracture Mechanics 192, 176–191.
[36] Javili, A., Morasata, R., Oterkus, E., Oterkus, S., 2019. Peridynamics review. Mathematics and Mechanics of Solids 24(11), 3714-3739.

[37] Silling, S.A., Epton, M., Weckner, O., Xu, J. and Askari, E., 2007. Peridynamic states and constitutive modeling. Journal of Elasticity, 88(2), pp.151-184.
[38] Silling, S.A. and Lehoucq, R.B., 2008. Convergence of peridynamics to classical elasticity theory. Journal of Elasticity, 93(1), p.13.
[39] Gu, X., Madenci, E. and Zhang, Q., 2018. Revisit of non-ordinary state-based peridynamics. Engineering fracture mechanics, 190, pp.31-52.
[40] Sun, C.T. and Vaidya, R.S., 1996. Prediction of composite properties from a representative volume element. Composites science and Technology, 56(2), pp.171-179.
[41] Sun, C.T. and Chen, J.L., 1991. A micromechanical model for plastic behavior of fibrous composites. Composites Science and Technology, 40(2), pp.115-129.
[42] Whitney, J.M. and Riley, M.B., 1966. Elastic properties of fiber reinforced composite materials. AIAA Journal, 4(9), pp.1537-1542.
[43] Markenscoff, X. and Dascalu, C., 2012. Asymptotic homogenization analysis for damage amplification due to singular interaction of micro-cracks. Journal of the Mechanics and Physics of Solids, 60(8), pp.1478-1485.